

Geometry-Controlled Excitonic Emission Engineering in Monolayer MoS₂ Using Plasmonic Hollow Nanocavities

Abdullah Efe Yildiz^{1,2} and Emre Ozan Polat^{1,2,*}

¹*Department of Physics, Bilkent University, 06800, Ankara, Turkey*

²*UNAM - National Nanotechnology Research Center and Institute of Materials Science and Nanotechnology, Bilkent University, Ankara 06800, Turkey*

**Corresponding author: emre.polat@bilkent.edu.tr*

Abstract

Spectral control of closely spaced excitonic transitions is essential for valleytronic photonics, nanoscale light sources, and wavelength-encoded sensing. In monolayer molybdenum disulfide (MoS₂), the A and B excitons are separated by only tens of meV, making spectral engineering both fundamentally important and technologically challenging. Here, we numerically investigate plasmon-enhanced excitonic emission in MoS₂ coupled to vertically oriented hollow gold nanocylindrical cavities separated by a dielectric spacer. Finite-difference time-domain simulations combined with a photoluminescence-rate framework allow independent evaluation of excitation enhancement, radiative decay modification, non-radiative quenching, and excitonic charge generation. By tuning the cavity aspect ratio, the localized surface plasmon resonance is aligned with either the A or B excitonic transition, while spacer thickness and refractive index regulate near-field confinement and the local density of optical states. Under optimized conditions, excitation rates reach 4.34-fold enhancement while radiative decay exceeds 40-fold, producing photoluminescence increases of 143.85 and 87.27 times for the A and B excitons. The cavity also redistributes the relative intensities of the excitonic peaks, yielding normalized exciton peak ratios up to 2.4 compared to bare MoS₂. These results establish hollow plasmonic nanocavities as a geometry-tunable platform for controlling excitonic emission and charge generation in atomically thin semiconductors.

Keywords: Monolayer MoS₂; Plasmonic nanocavities; Exciton-plasmon coupling; Purcell enhancement; Photoluminescence enhancement

Introduction

Two-dimensional transition metal dichalcogenides (TMDCs) provide a unique platform for nanoscale optoelectronics owing to their strong light-matter interactions and tightly bound excitons that remain stable at room temperature [1, 2]. In monolayer MoS₂, the direct bandgap at the K and K' valleys together with spin-orbit splitting of the valence band gives rise to spectrally distinct A and B excitons [3-5]. These excitonic transitions dominate the optical response and underpin applications in light-emitting devices, photodetectors, and valleytronic systems[6-8]. However, despite their large oscillator strengths, the atomic thickness of monolayer MoS₂ fundamentally limits optical absorption and emission [9, 10]. Rapid nonradiative decay and weak out-coupling to the far field suppress the external photoluminescence (PL) quantum yield, creating a practical bottleneck for device performance [11, 12]. Engineering the local electromagnetic environment is therefore essential to translate intrinsic excitonic strength into experimentally measurable emission and photocurrent enhancement [13, 14].

Plasmonic nanostructures offer a scalable and experimentally accessible route to manipulate emission by concentrating electromagnetic fields and modifying the local density of optical states (LDOS) [15, 16]. Gold nanoantennas and gap resonators integrated with MoS₂ have demonstrated enhanced PL and excitation-rate amplification via near-field confinement and Purcell-enhanced radiative recombination [17, 18]. Yet, most reported geometries rely on planar or solid metallic elements that predominantly generate lateral hotspots, limiting control over out-of-plane confinement and three-dimensional cavity modes [14, 19]. Hollow and coaxial metallic nanocavities, readily fabricated via template-assisted growth or galvanic replacement, support hybrid radial-longitudinal plasmon modes with deeply subwavelength mode volumes and geometry-dependent spectral tunability [20-22]. Despite their well-established synthesis and strong electromagnetic field confinement, hollow plasmonic nanocavities have only been sparsely explored for spectrally controlling excitonic emission in atomically thin semiconductors.

Here, we present a vertically oriented hollow gold nanocavity platform integrated with a dielectric spacer on monolayer MoS₂ on a device substrate (Si/SiO₂/MoS₂). Our structure is specifically tailored for geometry-controlled exciton-plasmon coupling. The coaxial cavity supports confined out-of-plane plasmon modes whose spectral position can be tuned through aspect ratio and wall thickness to overlap selectively with either the A or B exciton. Using finite-difference time-domain (FDTD) simulations combined with a PL and excitonic charge-generation analysis directly linked to experimentally measurable PL and carrier-generation rates, we systematically investigate the influence of cavity geometry and spacer thickness (Al₂O₃ or Polymethylmethacrylate (PMMA)). We demonstrate geometry-controlled enhancement of distinct excitonic transitions together with corresponding increases in electron-hole pair generation rates. While our numerical results

provide a realistic pathway toward spectrally programmable emission and photocurrent control, introducing hollow plasmonic nanocavities as a geometry-addressable degree of freedom for exciton selection establishes a fundamentally new three-dimensional cavity paradigm for transition-specific control of light emission and charge generation in atomically thin semiconductors.

Results

Figure 1 demonstrates the geometric tunability and spectral selectivity of the gold hollow nanocylinder (AuHNC) platform designed for exciton-plasmon coupling with monolayer (ML) MoS₂. The investigated structure is shown in **Figure 1a**, consisting of a hollow AuHNC with height H , outer radius R_o , and inner radius R_i placed on a dielectric spacer. To determine the spectral response of the cavities prior to integration with ML MoS₂, extinction cross-section spectra were calculated under broadband plane-wave excitation (400-800 nm).

As shown in **Figure 1b**, increasing the effective cavity aspect ratio (CAR), which reflects the effective cavity depth relative to the wall thickness that governs hybrid radial-longitudinal plasmon confinement,

$$CAR = \frac{H}{R_o - R_i} \quad (1)$$

induces a pronounced redshift of the localized surface plasmon resonance (LSPR). This behavior arises from geometry-driven plasmon hybridization between radial and axial cavity modes. The hollow configuration supports coupled charge oscillations on both the inner and outer metal surfaces, resulting in enhanced near-field confinement compared to solid gold nanostructures (**Supplementary Figure S1**). This dual interface mode coupling provides an additional degree of freedom for spectral engineering.

From this parametric study, two optimized geometries were selected to target the intrinsic excitonic resonances of ML MoS₂: $100 \times 50 \times 30 \text{ nm}$ ($CAR = 5$) aligned with the A exciton $100 \times 50 \times 20 \text{ nm}$ ($CAR = 3.33$) aligned with the B exciton. These dimensions ensure controlled spectral overlaps while preserving moderate linewidths suitable for weak-coupling conditions (**Figure 1b**).

Figures 1c and **d** show the effect of spacer thickness on the plasmonic response of the optimized AuHNC geometries on Al₂O₃ and PMMA spacers. As the spacer thickness increases from 2 to 25 nm, the dominant LSPR mode exhibits a clear and monotonic redshift in both dielectric systems.

This behavior reflects the progressive reduction of plasmon-substrate coupling and the effective modification of the local dielectric environment experienced by the near field.

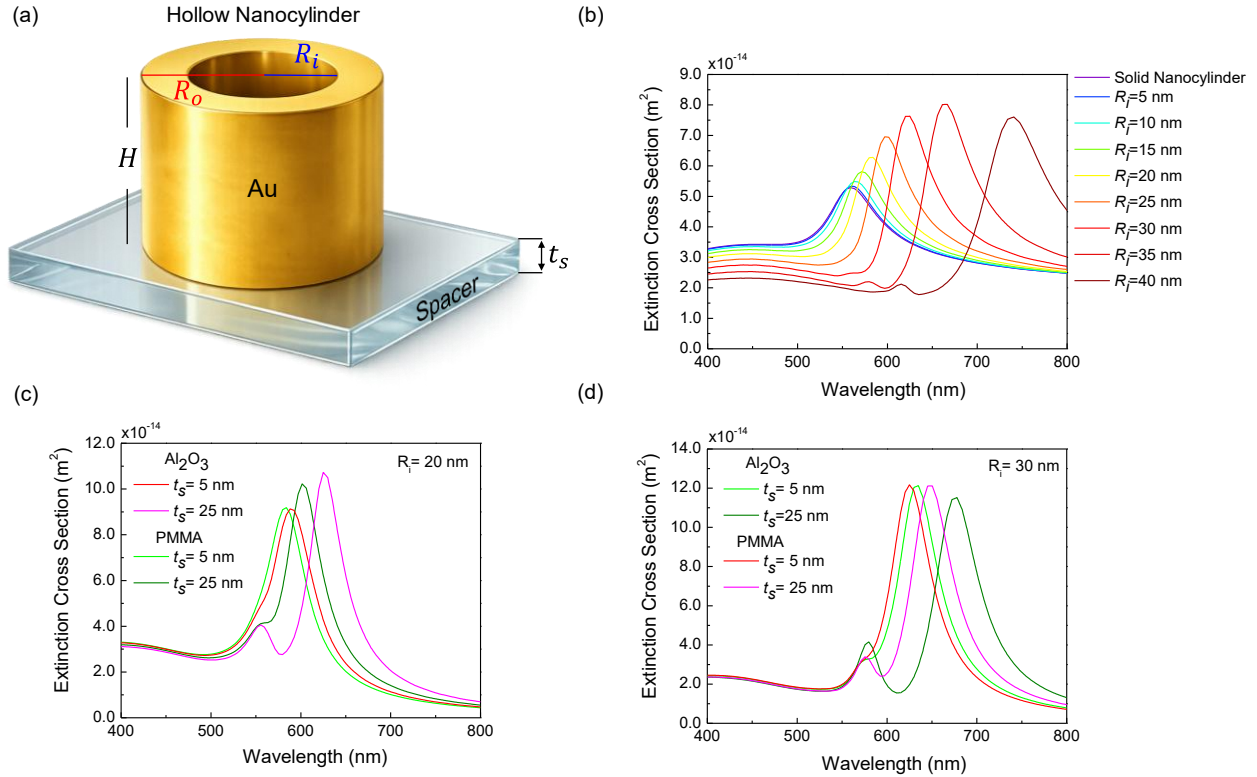


Figure 1. Geometry-controlled plasmonic tuning and spacer-dependent LSPR evolution in gold hollow nanocylinders (AuHNCs). (a) Schematic illustration of the AuHNC with height H , outer radius R_o , and inner radius R_i positioned on a dielectric spacer. (b) Calculated extinction cross-section spectra under broadband illumination (400-800 nm) for varying R_i . Systematic redshift of the dominant localized surface plasmon resonance (LSPR) with increasing CAR allows determination of the optimal geometry for specific wavelengths. (c) Extinction cross section spectra for the optimal AuHNC geometries with $R_i = 20$ nm and (d) $R_i = 30$ nm targeting for B and A excitons respectively. The primary LSPR mode exhibits a clear monotonic redshift with increasing spacer thickness for both types of spacers, consistent with reduced plasmon-substrate coupling and dielectric screening effects, while the higher-energy secondary mode remains largely insensitive to spacer variation.

For the A-exciton-targeted AuHNC geometry ($100 \times 50 \times 30$ nm ($CAR = 5$)), the LSPR peak exhibits a pronounced thickness-dependent redshift. Across the investigated spacer thickness range (5-25 nm), the resonance shifts by 54.4 nm for Al_2O_3 and 26.9 nm for PMMA spacers (Figure 1c,d

and **Supplementary Figure S1**). A comparable systematic redshift is also observed for the B-exciton-targeted geometry, where the LSPR peak shifts by 49.7 nm for Al₂O₃ and 19.3 nm for PMMA (See **Table 1**).

Table 1. Spacer-thickness-dependent evolution of the LSPR peaks of AuHNC relative to the A- and B-excitonic transitions of ML MoS₂. The table summarizes the LSPR peak wavelengths, the corresponding spectral shifts with respect to bare AuHNCs, and the full width at half maximum (FWHM) values for two spacer materials (Al₂O₃ and PMMA) with thicknesses ranging from 5 to 25 nm.

$R_i = 30 \text{ nm}$	LSPR Peak, λ_1 (nm)		Peak Shift, $\Delta\lambda$ (nm)		FWHM (nm)	
Spacer Thickness (nm)	Al ₂ O ₃	PMMA	Al ₂ O ₃	PMMA	Al ₂ O ₃	PMMA
5	634.9	625	11.4	1.5	58.9	58.4
10	650.4	634.9	26.9	11.4	59.6	59
15	661.2	640	37.7	16.5	60.2	58.7
20	666.7	645.1	43.2	21.6	61.4	59
25	677.9	650.4	54.4	26.9	62.1	59.4
$R_i = 20 \text{ nm}$	LSPR Peak, λ_1 (nm)		Peak Shift, $\Delta\lambda$ (nm)		FWHM (nm)	
Spacer Thickness (nm)	Al ₂ O ₃	PMMA	Al ₂ O ₃	PMMA	Al ₂ O ₃	PMMA
5	588.2	584	5.5	1.3	72.3	66.6
10	601.5	588.2	18.8	5.5	61.9	65.9
15	615.4	597	32.7	14.3	57	61.3
20	620.2	601.5	37.5	18.8	53.1	57.6
25	632.4	602	49.7	19.3	51.5	55.5

In both cases, the larger spectral shift observed for Al₂O₃ arises from its higher refractive index relative to PMMA, which enhances the dielectric contrast at the metal-dielectric interface and increases the near-field sensitivity of the plasmonic mode. This thickness-dependent spectral evolution is consistent with a simplified sensing-volume model, in which the plasmon resonance wavelength scales with the effective refractive index experienced within the evanescent near-field decay length [23, 24]:

$$\Delta\lambda = m\Delta n[1 - e^{-2d/l_d}] \quad (2)$$

where d is the spacer thickness, l_d is the evanescent field decay length, m is the bulk refractive-index sensitivity of the plasmon mode, and Δn represents the refractive-index contrast introduced by the spacer. The exponential term captures the finite spatial extent of the plasmonic near field,

leading to saturation behavior at larger separations. In contrast, the secondary high-energy resonance wavelength remains largely insensitive to spacer thickness, exhibiting only minor shifts of a few nanometers. This weak dependence indicates that this mode is dominated by localized charge oscillations confined to the cavity walls, with limited interaction volume extending into the surrounding dielectric. Consistent with this interpretation, the absence of significant linewidth broadening confirms that the observed spectral shifts originate primarily from dielectric screening effects rather than modifications of plasmon damping or radiative losses.

Figure 2 presents the absorption spectra of the AuHNC-MoS₂ hybrid system for Al₂O₃ and PMMA spacers with varying thicknesses, revealing the combined contributions of plasmonic and excitonic absorption processes. The investigated AuHNC array has an in-plane periodicity of 200 nm, and the corresponding unit cell configuration is shown in **Figure 2a**.

Figure 2b first establishes the dielectric-dependent plasmon-exciton interaction by comparing the absorption spectra of bare ML MoS₂ with those of the hybrid structure (MoS₂ + spacer + AuHNC) for Al₂O₃ and PMMA spacers. Here, the AuHNC geometry is defined by an inner radius of 20 nm, corresponding to an aspect ratio optimized for spectral proximity to the B-exciton transition. In the absence of the nanocavity, ML MoS₂ exhibits weak but distinct A and B excitonic absorption features. Upon integration with the AuHNC and dielectric spacer, a pronounced enhancement of the absorption near the B-exciton resonance emerges. Importantly, the magnitude and spectral alignment of this enhancement differ for Al₂O₃ and PMMA, reflecting the influence of the spacer refractive index on the LSPR energy and the resulting plasmon-exciton overlap. The higher refractive index of Al₂O₃ induces a stronger redshift of the LSPR compared with PMMA, leading to improved spectral alignment with the B-exciton and consequently stronger absorption enhancement.

Building on the dielectric comparison in **Figure 2b**, **Figures 2c** and **2d** investigate the spacer-thickness-dependent absorption response for two distinct AuHNC geometries defined by inner radii of $R_i = 20 \text{ nm}$ and $R_i = 30 \text{ nm}$, corresponding to abovementioned *CAR* values engineered to selectively target the B and A excitonic transitions of ML MoS₂ respectively. By increasing the inner radius from 20 nm to 30 nm while keeping the outer dimensions fixed, the primary LSPR systematically redshifts, enabling spectral alignment with either the higher-energy B-exciton or the lower-energy A-exciton.

For the $R_i = 20 \text{ nm}$ cavity (B-exciton-targeted geometry), the plasmonic mode spectrally overlaps with the B-exciton transition, leading to enhanced absorption predominantly around the B-exciton energy. In contrast, for the $R_i = 30 \text{ nm}$ cavity (A-exciton-targeted geometry), the redshifted LSPR aligns with the A-Exciton resonance, resulting in selective amplification of the A-exciton

absorption feature. In both geometries, the broadband background originates from Ohmic dissipation in gold, while the enhanced and spectrally localized features arise from plasmon-mediated field concentration at the MoS₂ plane.

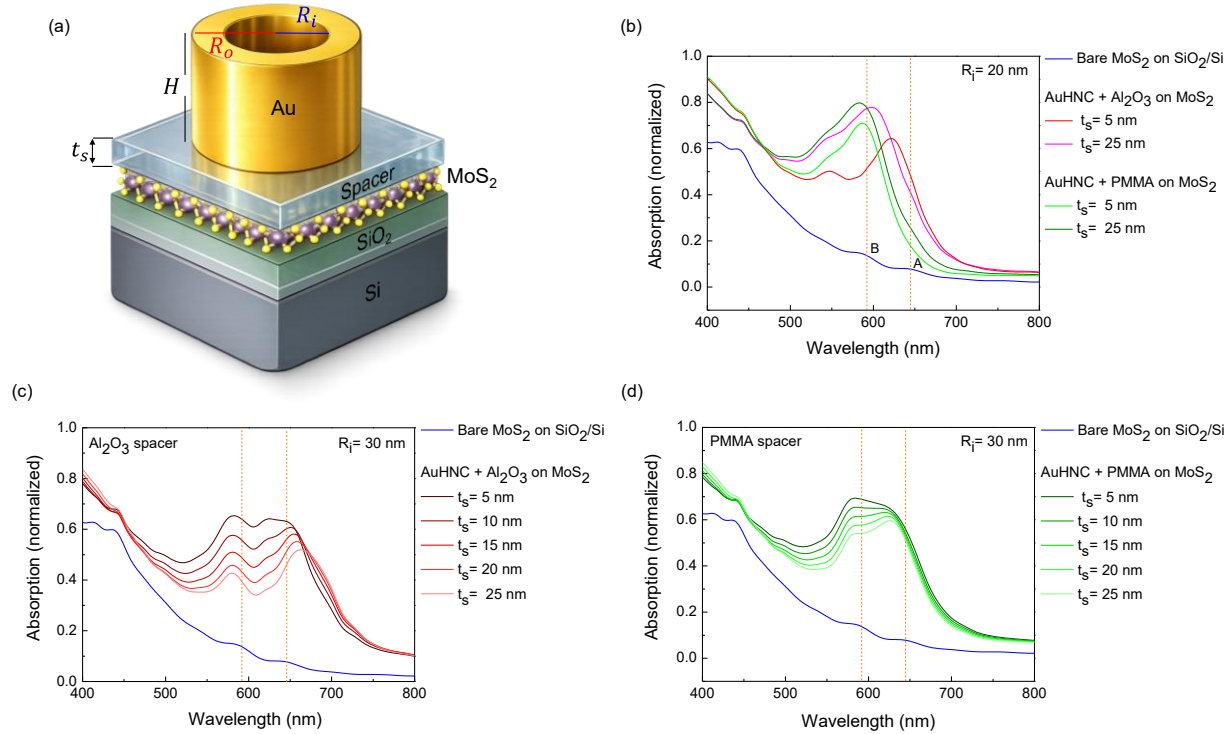


Figure 2. Exciton-aligned absorption response of AuHNC-MoS₂ hybrid nanostructures. (a) Schematic of the simulated unit cell consisting of ML MoS₂ supported on a SiO₂/Si substrate and separated from a periodic array (200 nm pitch) of gold hollow nanocylinders (AuHNCs) by a dielectric spacer of thickness t_s . The nanocavity geometry is defined by fixed outer dimensions and variable inner radius (R_i). (b) Absorption spectra of bare ML MoS₂ and the corresponding hybrid structures (MoS₂ + spacer + AuHNC) for Al₂O₃ and PMMA spacers, using an AuHNC with inner radius $R_i = 20$ nm (B-exciton-targeted geometry). The spectra highlight dielectric-dependent spectral alignment of the localized surface plasmon resonance (LSPR) with the B (X_B) excitonic transition and the resulting absorption enhancement. (c) Spacer-thickness-dependent absorption spectra (5–25 nm) for the hybrid structure incorporating an AuHNC with $R_i = 20$ nm, engineered for spectral overlap with the B-exciton and (d) for an AuHNC with $R_i = 30$ nm (A-exciton-targeted geometry). The individual redshifted LSPRs align with the B and A excitonic transitions, enabling selective enhancement of absorption while maintaining spectrally fixed exciton energies, consistent with weak-coupling behavior.

The enhancement mechanism is governed by strong electromagnetic field confinement associated with the primary LSPR mode, which increases the LDOS experienced by the excitonic dipoles. Despite the atomically thin nature of monolayer MoS₂, this near-field localization substantially amplifies excitonic absorption.

Spacer thickness further modulates this effect by regulating the spatial overlap between the evanescent plasmonic field and the excitonic layer. For thinner spacers (5 nm), the MoS₂ resides within the high-intensity near-field region, yielding pronounced enhancement of excitonic absorption. As the spacer thickness increases to 25 nm, the enhancement progressively diminishes due to the exponential decay of the plasmonic near field, while the intrinsic exciton energies remain spectrally fixed (**Supplementary Figure S2**). This behavior confirms that the system operates in the weak-coupling regime, where selective excitation enhancement is governed by spectral alignment and LDOS modulation rather than plasmon-exciton hybridization, as evidenced by the absence of excitonic energy shifts or Rabi splitting in the spectra. To directly quantify plasmon-enhanced excitation in the hybrid structures discussed in **Figure 2**, we evaluate the charge generation rate (CGR) in the monolayer MoS₂, which corresponds to the rate of electron-hole pair generation induced by optical absorption. In the numerical framework, CGR is computed using the imaginary dielectric function of ML MoS₂ (details are provided in the **Methodology** section). The CGR is extracted using an in-plane electric-field monitor positioned at the MoS₂ layer so that only the tangential electric-field components responsible for carrier generation are included.

Figure 3 summarizes the exciton-resolved CGR response of the AuHNC-MoS₂ hybrid system. The unit-cell geometry of the periodic AuHNC array integrated with the spacer-MoS₂-substrate stack is illustrated in **Figure 3a**. Two different nanocavity geometries are considered, corresponding to inner radii of $R_i = 20$ nm and $R_i = 30$ nm, which were previously shown in **Figure 2** to spectrally align the localized surface plasmon resonance (LSPR) with the B-exciton and A-exciton transitions of MoS₂, respectively. For the $R_i = 20$ nm cavity (**Figure 3b**), the plasmonic resonance overlaps predominantly with the B-exciton transition, leading to a pronounced increase in the CGR at this wavelength compared to the bare MoS₂ case. In contrast, the enhancement near the A-exciton remains comparatively weaker, indicating that this geometry preferentially amplifies the excitation of the B exciton. The magnitude of the enhancement is strongest for the smallest spacer separations where the MoS₂ layer resides within the intense evanescent plasmonic field. When the cavity inner radius is increased to $R_i = 30$ nm, the plasmonic resonance redshifts and becomes spectrally aligned with the A-exciton transition, as shown in **Figure 3b**. The **inset of Figure 3d** further compares the CGR spectra for Al₂O₃ and PMMA spacers at a fixed thickness of 2 nm, allowing the influence of the dielectric environment to be examined independently of spacer separation. The spectra show that both spacer materials produce nearly identical excitonic peak positions, confirming that the excitonic resonances are intrinsic to the MoS₂ layer. However, the

Al₂O₃ spacer yields a slightly stronger CGR enhancement compared with PMMA. This behavior originates from the higher refractive index of Al₂O₃, which induces a larger redshift of the plasmonic resonance and improves its spectral overlap with the A-exciton transition. Consequently, the plasmon-exciton coupling strength becomes marginally stronger for the Al₂O₃ spacer under otherwise identical geometrical conditions. As a result, the CGR spectrum exhibits a strong enhancement around the A-exciton wavelength while the B-exciton enhancement becomes relatively weaker (**Supplementary Figure S3**). This spectral redistribution confirms that the plasmonic cavity geometry can be used to selectively enhance different excitonic transitions in monolayer MoS₂.

The exciton-specific enhancement factors extracted from the CGR spectra are summarized in **Figures 3c** and **3d**, where the results for Al₂O₃ (red) and PMMA (green) spacers are shown separately. For the $R_i = 20$ nm geometry, the B-exciton enhancement reaches 3.94 for Al₂O₃ and 3.67 for PMMA at the smallest spacer thickness of 2 nm (**Figure 3c**). As the spacer thickness increases, the enhancement gradually decreases for both spacer materials, approaching unity at larger separations as the plasmonic near-field interaction weakens. In contrast, for the $R_i = 30$ nm cavity, the A-exciton enhancement reaches 4.34 for Al₂O₃ and 4.1 for PMMA, indicating stronger excitation enhancement compared with the B-exciton-targeted geometry. The enhancement again decreases with increasing spacer thickness due to the exponential decay of the plasmonic near field sampled at the MoS₂ plane. Taken together, these results demonstrate that the inner radius of the AuHNC cavity provides a direct geometrical handle to enhance different excitonic transitions in monolayer MoS₂.

Although the CGR enhancement quantifies the efficiency of plasmon-assisted exciton generation, it does not directly determine the observed PL intensity. The detected PL depends on both the excitation rate and the balance between radiative and non-radiative decay processes. In plasmonic environments, near-field enhancement can simultaneously increase excitation while also introducing additional non-radiative energy-transfer pathways to the metal. Therefore, achieving net PL enhancement (*P**L**E*) requires optimizing both the excitation enhancement and the emission efficiency. For materials with intrinsically low quantum yield such as monolayer MoS₂ ($\eta_0 \approx 10^{-3}$ - 10^{-4}), the *P**L**E* can be approximated as [25, 26]

$$P L E \approx \left| \frac{G}{G_0} \right| \times F_{rad} \quad (3)$$

where G/G_0 represents the CGR (excitation) enhancement factor and F_{rad} is the normalized radiative decay rate of the hybrid system. The radiative and non-radiative decay rates are calculated

using an in-plane dipole model for the MoS₂ exciton interacting with the plasmonic nanocavity, allowing the quantum efficiency of the hybrid structure to be expressed as

$$QE = \frac{F_{rad}}{F_{rad} + F_{nonrad}} \quad (4)$$

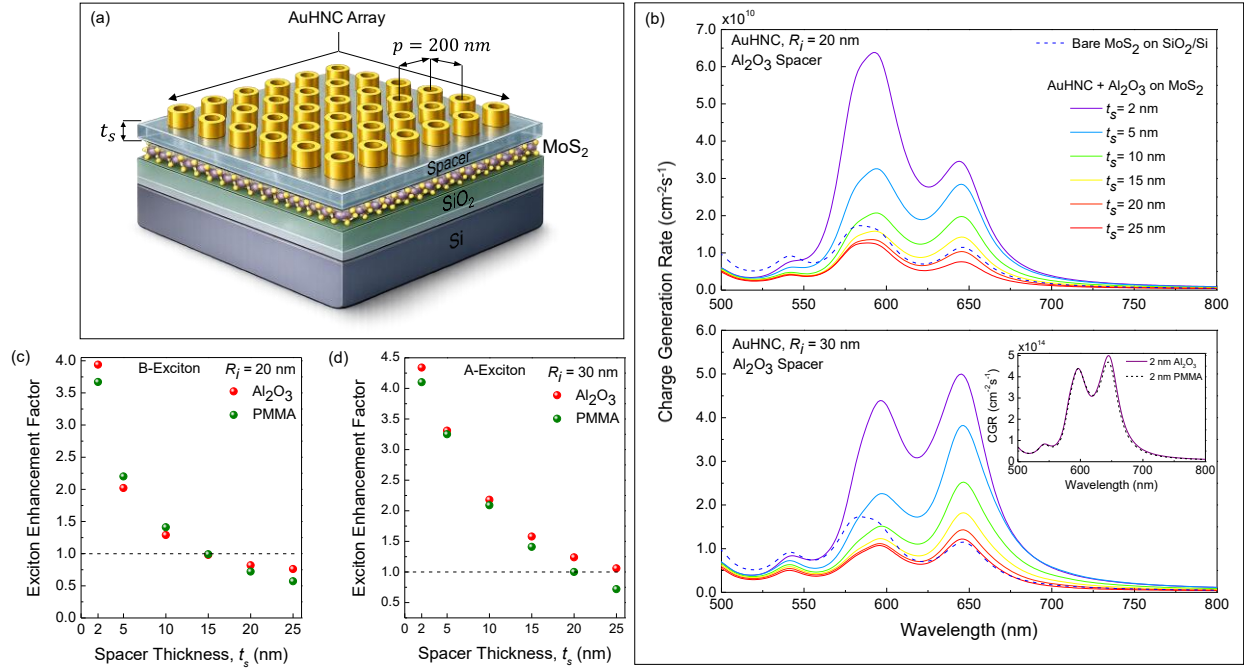


Figure 3. Plasmon-enhanced exciton charge generation in AuHNC-MoS₂ hybrid nanostructures. (a) Schematic of the simulated periodic Au hollow nanocylinder (AuHNC) array (periodicity $p = 200$ nm) separated from monolayer (ML) MoS₂ by a dielectric spacer of thickness t_s , supported on a SiO₂/Si substrate. (b) Charge generation rate (CGR) spectra for the $R_i = 20$ nm and $R_i = 30$ nm AuHNC geometries respectively using an Al₂O₃ spacer with thicknesses $t_s = 2$ -25 nm. The dashed curve corresponds to bare MoS₂ on the SiO₂/Si substrate. Inset: CGR spectra for 2 nm Al₂O₃ and PMMA spacers, highlighting the influence of the dielectric environment on the plasmon-exciton spectral overlap. (c) B-exciton enhancement factor extracted from the CGR spectra for the $R_i = 20$ nm AuHNC geometry as a function of spacer thickness for Al₂O₃ and PMMA (green) spacers. The enhancement reaches 3.94 for Al₂O₃ and 3.67 for PMMA at $t_s = 2$ nm, gradually decreasing toward unity as the spacer thickness increases due to the decay of the plasmonic near field. (d) A-exciton enhancement factor extracted from the CGR spectra for the $R_i = 30$ nm AuHNC geometry. At $t_s = 2$ nm, the enhancement reaches 4.34 for Al₂O₃ and 4.1 for PMMA, with the enhancement progressively diminishing for larger spacer thicknesses as the MoS₂ layer moves away from the region of strongest plasmonic field confinement.

Although quantifying plasmon-enhanced excitation rates through CGR spectra provides viable insights for the experimental implementations, the observable PL depends on the combined effects of excitation enhancement and modified emission dynamics. Therefore, in **Figure 4** we evaluate the resulting QE, PLE and exciton intensity redistribution of the AuHNC-MoS₂ hybrid system. **Figure 4a** demonstrates the QE maps of AuHNC-MoS₂ hybrid system with $R_i = 20$ nm and $R_i = 30$ nm and Al₂O₃ spacer (See **Supplementary Figure S4** for the PMMA counterpart). For the B-exciton targeted geometry ($R_i = 20$, shown in green color map), the QE is maximized near the intrinsic excitonic transition wavelengths of monolayer MoS₂, reaching the maximum value of 0.54 at 612 nm for 25 nm spacer thickness indicating that the plasmonic resonance efficiently couples to the emission channel of the B-exciton. Similarly, red colormap of **Figure 4a** shows the QE map for A-exciton targeted geometry ($R_i = 30$ nm and Al₂O₃ spacer). The maximum QE is recorded as 0.73 at 620 nm for 25 nm spacer thickness indicating stronger excitation enhancement compared with the B-exciton-targeted geometry in conjunction with the exciton enhancement factors reported in **Figure 3**. Note that the reported QE values represent the internal quantum efficiency of the hybrid system, not the external PL efficiency. As spacer thickness increases, non-radiative energy transfer to the metal is reduced, leading to higher QE values. However, the normalized radiative power simultaneously decreases with increasing separation and can undergo 6-fold reduction with respect to the bare ML MoS₂ radiative rate (**Table 2**). This highlights the need to optimize spacer thickness to balance radiative enhancement and non-radiative losses.

The resulting PL enhancement factors are displayed in **Figure 4b** (and **Table 2**), which shows the calculated PL enhancement for the B-exciton and A-exciton transitions, respectively. The AuHNC-MoS₂ hybrid structures exhibit significantly larger enhancement compared to previously reported plasmonic systems such as Au nanorods (~3 times) and nanospheres (~45 times) [25, 27-29]. The maximum *PLE* reaches 143.85-fold for the A-exciton and 87.27-fold for the B-exciton, substantially exceeding the typical enhancement factors reported for conventional plasmonic nanoparticles (generally below ~50-fold). This improvement originates from the strong electric-field confinement within the hollow nanocavity, which simultaneously enhances the excitation rate and the radiative decay channel.

An additional advantage of employing AuHNCS with tunable aspect ratios is their ability to modify the relative spectral contributions of the A and B excitonic transitions. To quantify this effect, we evaluate the normalized excitonic peak ratio (*NEPR*), defined as the ratio between the A and B excitonic peak intensities in the enhanced spectra normalized to the corresponding peak ratio of bare MoS₂. This metric therefore measures how the plasmonic cavity redistributes the excitonic emission balance relative to the intrinsic response of monolayer MoS₂. The resulting *NEPRs* are summarized in **Table 2** and plotted in **Figure 4c** for Al₂O₃ and PMMA spacers, respectively. For the $R_i = 30$ nm geometry, where the plasmonic resonance is aligned closer to the A-exciton

transition, the normalized ratio reaches values up to 2.4 for a 5 nm Al_2O_3 spacer, indicating that the A-exciton peak becomes more than twice as dominant relative to the B-exciton compared with the bare MoS_2 spectrum. A similar but slightly weaker redistribution is observed for the PMMA spacer where the ratio reaches a maximum of 1.9 across the investigated spacer thicknesses. In contrast, the $R_i = 20$ nm geometry, designed to interact more strongly with the B-exciton transition, yields normalized ratios closer to unity, indicating a more balanced enhancement of the two excitonic channels. These results show that AuHNC cavities do not simply provide broadband

enhancement but instead reshape the relative excitonic emission spectrum through geometry-dependent plasmon-exciton alignment. Such control over the relative intensities of excitonic transitions provides a practical route toward spectral engineering of excitonic emission in atomically thin semiconductors.

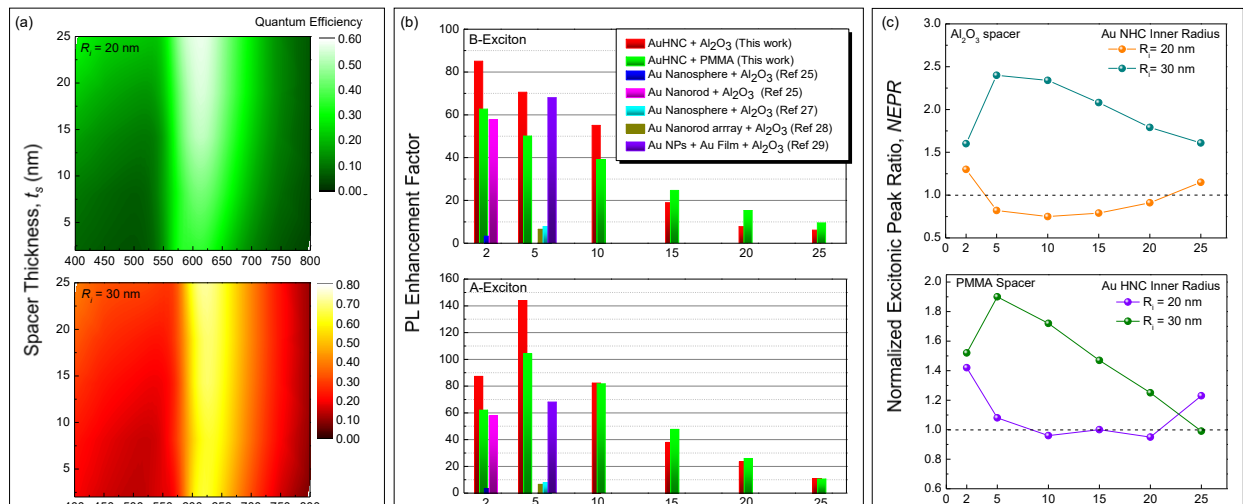


Figure 4. Quantum efficiency, PL enhancement and normalized excitonic peak ratios in AuHNC-MoS₂ hybrid structures. (a) *QE* maps as a function of wavelength and spacer thickness t_s for AuHNC geometries with inner radii $R_i = 20$ nm and $R_i = 30$ nm (Al_2O_3 spacer). The maximum *QE* occurs in the spectral region of the excitonic transitions, confirming that optimal radiative efficiency is achieved when the plasmonic resonance is aligned with the intrinsic A and B exciton energies (b) *PLE* factors at the B- and A-exciton wavelengths compared with previously reported plasmonic structures, shown as a function of spacer thickness for AuHNC structures with Al_2O_3 and PMMA spacers. Hollow nanocavities enable substantially larger photoluminescence enhancement, with *PLE* values reaching up to 145-fold in this work, representing up to 45-fold higher enhancement compared with previously reported plasmonic architectures. (c) *NEPR* plotted as a function of spacer thickness for Al_2O_3 (top) and PMMA (bottom) spacers for AuHNC inner radii $R_i = 20$ nm and $R_i = 30$ nm. Implemented cavity geometry enables controlled redistribution of the relative A and B excitonic contributions, showing that plasmonic nanocavities can spectrally reshape excitonic emission rather than merely amplify it.

Table 2 | Geometry- and spacer-dependent excitonic enhancement metrics in AuHNC-MoS₂ hybrid structures. Spacer-thickness-dependent excitation enhancement factors (G/G_0), normalized radiative decay rates (F_{rad}), PL enhancement (PLE), and the normalized excitonic peak ratio ($NEPR$) for the AuHNC–monolayer MoS₂ hybrid system. Results are reported for cavity geometries with inner radii $R_i = 30\text{nm}$ (A-exciton-aligned) and $R_i = 20\text{nm}$ (B-exciton-aligned) and for both Al₂O₃ and PMMA spacer layers. The $NEPR$ metric quantifies the redistribution of the relative A/B excitonic peak intensities compared with bare MoS₂.

$R_i = 30\text{ nm}$ (A-Exciton)	Excitation Enhancement Factor ($\frac{G}{G_0}$)		Normalized Radiative Decay Rate (F_{rad})		PL Enhancement (PLE)		Normalized excitonic peak ratio, ($NEPR$)	
	Al ₂ O ₃	PMMA	Al ₂ O ₃	PMMA	Al ₂ O ₃	PMMA	Al ₂ O ₃	PMMA
Spacer Thickness (nm)								
2	4.34	4.1	19.12	15.12	82.98	61.99	1.6	1.52
5	3.31	3.25	43.46	32.03	143.85	104.10	2.4	1.9
10	2.18	2.09	37.72	39.08	82.23	81.68	2.34	1.72
15	1.58	1.41	23.97	33.75	37.87	47.59	2.08	1.47
20	1.24	1	18.75	25.84	23.25	25.84	1.79	1.25
25	1.06	0.72	10.03	14.61	10.63	10.52	1.61	0.99
$R_i = 20\text{ nm}$ (B-Exciton)								
Spacer Thickness (nm)								
2	3.94	3.67	22.15	17.85	87.27	65.51	1.3	1.42
5	2.02	2.2	34.07	23.17	68.82	50.97	0.82	1.08
10	1.29	1.41	41.72	28.28	53.82	39.87	0.75	0.96
15	0.98	0.99	19.13	25.45	18.75	25.20	0.79	1
20	0.82	0.72	9.28	21.17	7.61	15.24	0.91	0.95
25	0.76	0.57	8.13	16.55	6.18	9.43	1.15	1.23

Conclusion, Discussion and Outlook

In this work, we demonstrate that vertically oriented AuHNCs provide an effective and tunable platform for enhancing excitonic emission in monolayer MoS₂ through controlled plasmon-exciton interactions. By engineering cavity geometry, the primary LSPR can be spectrally aligned with either the A or B excitonic transitions while maintaining operation in the weak-coupling regime. Systematic variation of the spacer thickness (2-25 nm) allows deterministic control of the plasmonic near-field overlap with the MoS₂ layer. For small separations, strong excitation

enhancement is observed, with charge generation rates reaching 4.34 and 3.94 times the bare MoS₂/substrate values for the A and B excitonic transitions, respectively. As the spacer thickness increases, the near-field interaction decays rapidly and the excitation enhancement approaches or falls below the bare MoS₂ limit beyond approximately 20-25 nm.

Importantly, our results show that excitation enhancement alone does not directly translate into increased PL. Instead, the overall PL enhancement is determined by the balance between plasmon-enhanced excitation and cavity-modified radiative decay. Under optimized cavity and spacer conditions, the AuHNC-MoS₂ hybrid system achieves *P**L**E* of up to 143.85-fold for the A excitonic transition and 87.27-fold for the B-excitonic transition, exceeding enhancement levels typically reported for solid Au nanorods and nanospheres. In addition, the tunable cavity aspect ratio enables controlled redistribution of excitonic emission channels, producing *NEPRs* as high as 2.4 relative to bare MoS₂.

These results highlight the advantages of hollow coaxial plasmonic geometries, where hybrid radial-longitudinal modes provide strong field confinement and efficient local density of optical states engineering. Beyond fundamental plasmon-exciton coupling studies, this geometry-dependent design strategy offers a practical route for enhancing and spectrally shaping emission from low-quantum-yield 2D semiconductors. Such capabilities are particularly relevant for the development of ultrathin light sources, on-chip nanophotonic emitters, valleytronic devices, and integrated optoelectronic platforms based on atomically thin materials [30-33].

Methodology

To accurately capture both the atomistic excitonic response of monolayer MoS₂ and the electromagnetic field confinement of the plasmonic cavity, we combined first-principles excitonic calculations with full-wave electromagnetic simulations. The optical response of the MoS₂-Au hollow nanocavity system was simulated using the FDTD method.

The optical response of the MoS₂-Au hollow nanocavity system was simulated using the finite-difference time-domain (FDTD) method, which numerically solves Maxwell's equations in both space and time. In this approach, Maxwell's curl equations

$$\nabla \times \mathbf{E} = -\mu \frac{\partial \mathbf{H}}{\partial t} \quad (5)$$

$$\nabla \times \mathbf{H} = \varepsilon \frac{\partial \mathbf{E}}{\partial t} + \mathbf{J} \quad (6)$$

are discretized on a Yee grid, where \mathbf{E} and \mathbf{H} denote the electric and magnetic fields, μ is the magnetic permeability, ε is the permittivity, and \mathbf{J} is the induced current density. Perfectly matched

layers (PMLs) were applied at the simulation boundaries to emulate an open electromagnetic environment and suppress artificial reflections. All simulations were performed using a three-dimensional FDTD solver (Ansys Lumerical FDTD) with spatial and temporal discretization chosen to satisfy the Courant stability condition while resolving the nanoscale features of the MoS₂ layer and the plasmonic cavity.

The dispersive optical properties of the materials were implemented using experimentally validated refractive-index datasets. Gold was described using the Johnson and Christy data set [34], while Si, SiO₂, and Al₂O₃ were modeled using wavelength-dependent optical constants from the Palik Handbook [35-37]. PMMA was implemented as a transparent dielectric using its Sellmeier-type dispersion relation [38]

$$n^2(\lambda) = 1 + \frac{0.99654\lambda^2}{\lambda^2 - 0.00787} + \frac{0.18964\lambda^2}{\lambda^2 - 0.02191} + \frac{0.00411\lambda^2}{\lambda^2 - 3.85727} \quad (7)$$

which accurately reproduces its refractive index across the visible spectrum.

To evaluate the optical response of the plasmonic cavity, broadband extinction spectra were calculated using a total-field scattered-field (TFSF) plane-wave source spanning 400-800 nm. Absorption within the Au nanocavity and spacer layers was obtained by integrating the power dissipation density over their volumes, while scattering was calculated from the far-field power exiting the TFSF boundaries.

The optical response of monolayer MoS₂ was obtained from first-principles calculations using the density functional theory (DFT)-Bethe-Salpeter equation (BSE) framework. Ground-state electronic structure calculations were performed within the projector augmented-wave (PAW) method using the generalized gradient approximation (GGA) in the PBE form with a plane-wave cutoff of 500 eV and a $16 \times 16 \times 1$ Γ -centered k-point mesh [39, 40]. A vacuum spacing of 20 Å was applied along the out-of-plane direction to avoid interlayer interactions. Spin-orbit coupling was included to correctly capture the splitting between the A and B excitons. Quasiparticle corrections were calculated using the G₀W₀ approximation, followed by excitonic calculations within the BSE framework [41-43]. An energy cutoff of 150 eV was used for the response function.

The resulting complex dielectric function

$$\varepsilon(\omega) = \varepsilon_1(\omega) + i\varepsilon_2(\omega) \quad (8)$$

was implemented in the FDTD simulations as a surface conductivity layer according to

$$\sigma(\omega) = -i\omega t \varepsilon_0 [\varepsilon(\omega) - 1] \quad (9)$$

where ε_0 is the vacuum permittivity, ω is the angular frequency, and t is the effective monolayer thickness. The MoS₂ layer was modeled as an in-plane isotropic sheet conductivity, consistent with the dominant in-plane excitonic response of monolayer TMDCs.

Charge-generation rates were calculated from the spatially resolved electromagnetic fields. Under optical excitation, the local absorption in the MoS₂ layer is given by the power dissipation density

$$P(\mathbf{r}, \lambda) = \frac{1}{2} \omega \varepsilon_0 \varepsilon_2(\mathbf{r}, \lambda) |\mathbf{E}(\mathbf{r}, \lambda)|^2 \quad (10)$$

The corresponding electron-hole pair generation rate is

$$G(\mathbf{r}, \lambda) = \frac{P(\mathbf{r}, \lambda)}{\hbar \omega} = \frac{1}{2} \frac{\omega \varepsilon_0 \varepsilon_2 |\mathbf{E}|^2}{\hbar \omega} \quad (11)$$

The generation maps were integrated over the MoS₂ plane to obtain wavelength-dependent CGR spectra.

Radiative and non-radiative decay rates were evaluated by modeling the MoS₂ exciton as an in-plane oscillating electric dipole located near the plasmonic cavity. In free space, the intrinsic dipole decay rate is given by [44]

$$\gamma_0 = \frac{\omega^3 |p|^2}{3\pi \varepsilon_0 \hbar c^3} \quad (12)$$

where p is the dipole moment and c is the speed of light. Within the cavity environment, the total decay rate was obtained from the total emitted power

$$\gamma_{tot} = \frac{P_{tot}}{P_0} \gamma_0 \quad (13)$$

where P_0 is the dipole power in free space. Radiative emission was determined using far-field monitors,

$$\gamma_{rad} = \frac{P_{rad}}{P_0} \gamma_0 \quad (14)$$

while the non-radiative decay rate associated with metallic losses was obtained as:

$$\gamma_{nonrad} = \gamma_{tot} - \gamma_{rad}. \quad (15)$$

Near-field monitors were used to capture the full Poynting-vector flux surrounding the emitter,

$$P_{tot} = \oint \mathbf{S} \cdot d\mathbf{A} \quad (16)$$

whereas far-field projection monitors were used to evaluate

$$P_{rad} = \oint_{far} \mathbf{S} \cdot d\mathbf{A}. \quad (17)$$

This framework allows a clear separation of radiative enhancement and non-radiative plasmonic losses and enables quantitative evaluation of cavity-modified decay dynamics.

Acknowledgments

E.O.P. acknowledges financial support from the Scientific and Technological Research Council of Türkiye (TÜBİTAK) through Grant No. 222N308 within the CHIST-ERA program. Additional support was provided by the Turkish Academy of Sciences Outstanding Young Scientists Awards (GEBİP) 2025.

Author Contributions

A.E.Y. performed the numerical simulations, carried out the calculations, and extracted the raw data underlying the reported results. A.E.Y. also contributed to the preparation of the manuscript. E.O.P. conceived the research idea, supervised the project, and led the preparation of the manuscript, including the development of the final figures and the main text. All authors discussed the results and contributed to the final version of the manuscript.

Competing Interests

The authors declare no competing financial or non-financial interests.

Data Availability

All data necessary to evaluate the conclusions of this work are included in the paper and the supplementary information. Additional datasets supporting the findings of this study are available from the corresponding author upon reasonable request.

References

- [1] G. Wang *et al.*, “Colloquium: Excitons in atomically thin transition metal dichalcogenides,” *Rev. Mod. Phys.*, vol. 90, no. 2, p. 021001, 2018.
- [2] K. He *et al.*, “Tightly bound excitons in monolayer WSe₂,” *Phys. Rev. Lett.*, vol. 113, no. 2, p. 026803, 2014.
- [3] K. F. Mak, C. Lee, J. Hone, J. Shan, and T. F. Heinz, “Atomically thin MoS₂: A new direct-gap semiconductor,” *Phys. Rev. Lett.*, vol. 105, no. 13, p. 136805, 2010.
- [4] A. Splendiani *et al.*, “Emerging photoluminescence in monolayer MoS₂,” *Nano Lett.*, vol. 10, no. 4, pp. 1271–1275, 2010.
- [5] D. Xiao, G. Liu, W. Feng, X. Xu, and W. Yao, “Coupled spin and valley physics in monolayers of MoS₂ and other group-VI dichalcogenides,” *Phys. Rev. Lett.*, vol. 108, no. 19, p. 196802, 2012.
- [6] O. Lopez-Sanchez, D. Lembke, M. Kayci, A. Radenovic, and A. Kis, “Ultrasensitive photodetectors based on monolayer MoS₂,” *Nat. Nanotechnol.*, vol. 8, no. 7, pp. 497–501, 2013.
- [7] J. S. Ross *et al.*, “Electrical control of neutral and charged excitons in a monolayer semiconductor,” *Nat. Commun.*, vol. 4, p. 1474, 2013.
- [8] H. Zeng, J. Dai, W. Yao, D. Xiao, and X. Cui, “Valley polarization in MoS₂ monolayers by optical pumping,” *Nat. Nanotechnol.*, vol. 7, no. 8, pp. 490–493, 2012.
- [9] W. Zheng *et al.*, “Light emission properties of 2D transition metal dichalcogenides: Fundamentals and applications,” *Adv. Opt. Mater.*, vol. 6, no. 21, p. 1800420, 2018.
- [10] N. Ansari and F. Ghorbani, “Light absorption optimization in two-dimensional transition metal dichalcogenide van der Waals heterostructures,” *J. Opt. Soc. Am. B*, vol. 35, no. 5, pp. 1179–1185, 2018.
- [11] M. Amani *et al.*, “Near-unity photoluminescence quantum yield in MoS₂,” *Science*, vol. 350, no. 6264, pp. 1065–1068, 2015.
- [12] G. Eda and S. A. Maier, “Two-dimensional crystals: Managing light for optoelectronics,” *ACS Nano*, vol. 7, no. 7, pp. 5660–5665, 2013.
- [13] R. S. Sundaram *et al.*, “Electroluminescence in single-layer MoS₂,” *Nano Lett.*, vol. 13, no. 4, pp. 1416–1421, 2013.
- [14] B. Lee *et al.*, “Fano resonance and spectrally modified photoluminescence enhancement in monolayer MoS₂ integrated with plasmonic nanoantenna arrays,” *Nano Lett.*, vol. 15, no. 5, pp. 3646–3653, 2015.
- [15] P. Lunnemann and A. F. Koenderink, “The local density of optical states of a metasurface,” *Sci. Rep.*, vol. 6, p. 20655, 2016.
- [16] S. Jin *et al.*, “Plasmonic tuning of dark-exciton radiation dynamics and far-field emission directionality in monolayer WSe₂,” *Sci. Adv.*, vol. 12, no. 3, p. eaea5781, 2026.

- [17] P. Bharadwaj, B. Deutsch, and L. Novotny, "Optical antennas," *Adv. Opt. Photon.*, vol. 1, no. 3, pp. 438–483, 2009.
- [18] M. S. Tame *et al.*, "Quantum plasmonics," *Nat. Phys.*, vol. 9, no. 6, pp. 329–340, 2013.
- [19] S. Butun, S. Tongay, and K. Aydin, "Enhanced light emission from large-area monolayer MoS₂ using plasmonic nanodisc arrays," *Nano Lett.*, vol. 15, no. 4, pp. 2700–2704, 2015.
- [20] A. Moreau *et al.*, "Controlled-reflectance surfaces with film-coupled colloidal nanoantennas," *Nature*, vol. 492, no. 7427, pp. 86–89, 2012.
- [21] W. Zhang, J. Yang, and X. Lu, "Tailoring galvanic replacement reaction for the preparation of Pt/Ag bimetallic hollow nanostructures with controlled number of voids," *ACS Nano*, vol. 6, no. 8, pp. 7397–7405, 2012.
- [22] Y. Sun and Y. Xia, "Shape-controlled synthesis of gold and silver nanoparticles," *Science*, vol. 298, no. 5601, pp. 2176–2179, 2002.
- [23] M. E. Stewart *et al.*, "Multispectral thin-film biosensing and quantitative imaging using 3D plasmonic crystals," *Anal. Chem.*, vol. 81, no. 15, pp. 5980–5989, 2009.
- [24] I. Kaminska *et al.*, "Near-field and far-field sensitivities of LSPR sensors," *J. Phys. Chem. C*, vol. 119, no. 17, pp. 9470–9476, 2015.
- [25] M. Garai *et al.*, "Single-particle studies on plasmon-enhanced photoluminescence of monolayer MoS₂ by gold nanoparticles of different shapes," *J. Chem. Phys.*, vol. 155, no. 23, p. 234201, 2021.
- [26] W. Zhao *et al.*, "Exciton-plasmon coupling and electromagnetically induced transparency in monolayer semiconductors hybridized with Ag nanoparticles," *Adv. Mater.*, vol. 28, no. 14, pp. 2709–2715, 2016.
- [27] X. Qi *et al.*, "Effects of gap thickness and emitter location on the photoluminescence enhancement of monolayer MoS₂ in a plasmonic nanoparticle-film coupled system," *Nanophotonics*, vol. 9, no. 7, pp. 2097–2105, 2020.
- [28] K. Lee *et al.*, "Plasmonic gold nanorods coverage influence on enhancement of the photoluminescence of two-dimensional MoS₂ monolayer," *Sci. Rep.*, vol. 5, p. 16374, 2015.
- [29] Y. Huang *et al.*, "High-enhancement photoluminescence of monolayer MoS₂ in hybrid plasmonic systems," *Appl. Opt.*, vol. 63, no. 10, pp. 2704–2709, 2024.
- [30] K. Nielsen *et al.*, "Programmable nonlinear quantum photonic circuits," *Nat. Commun.*, vol. 16, no. 1, p. 11397, 2025.
- [31] E. O. Polat, H. Uzlu, O. Balci, N. Kakenov, E. Kovalska, and C. Kocabas, "Graphene-enabled optoelectronics on paper," *ACS Photonics*, vol. 3, no. 6, pp. 964–971, 2016.
- [32] E. O. Polat *et al.*, "Flexible graphene photodetectors for wearable fitness monitoring," *Sci. Adv.*, vol. 5, no. 9, p. eaaw7846, 2019.

- [33] I. Tyulnev *et al.*, “Valleytronics in bulk MoS₂ with a topologic optical field,” *Nature*, vol. 628, no. 8009, p. 690, 2024.
- [34] P. B. Johnson and R. W. Christy, “Optical constants of the noble metals,” *Phys. Rev. B*, vol. 6, no. 12, pp. 4370–4379, 1972.
- [35] D. F. Edwards, “Silicon (Si),” in *Handbook of Optical Constants of Solids*, E. D. Palik, Ed. New York: Academic Press, 1985, pp. 547–569.
- [36] F. Gervais, “Aluminum oxide (Al₂O₃),” in *Handbook of Optical Constants of Solids*, E. D. Palik, Ed. New York: Academic Press, 1998, pp. 761–775.
- [37] H. R. Philipp, “Silicon dioxide (SiO₂),” in *Handbook of Optical Constants of Solids*, E. D. Palik, Ed. New York: Academic Press, 1985, pp. 719–747.
- [38] N. Sultanova, S. Kasarova, and I. Nikolov, “Dispersion properties of optical polymers,” *Acta Phys. Pol. A*, vol. 116, no. 4, pp. 585–587, 2009.
- [39] P. E. Blöchl, “Projector augmented-wave method,” *Phys. Rev. B*, vol. 50, no. 24, pp. 17953–17979, 1994.
- [40] J. P. Perdew, K. Burke, and M. Ernzerhof, “Generalized gradient approximation made simple,” *Phys. Rev. Lett.*, vol. 77, no. 18, pp. 3865–3868, 1996.
- [41] M. S. Hybertsen and S. G. Louie, “Electron correlation in semiconductors and insulators: Band gaps and quasiparticle energies,” *Phys. Rev. B*, vol. 34, no. 8, pp. 5390–5413, 1986.
- [42] M. Shishkin and G. Kresse, “Self-consistent GW calculations for semiconductors and insulators,” *Phys. Rev. B*, vol. 75, no. 23, p. 235102, 2007.
- [43] L. Hedin, “New method for calculating the one-particle Green’s function with application to the electron-gas problem,” *Phys. Rev.*, vol. 139, no. 3A, pp. A796–A823, 1965.
- [44] A. Gulucu and E. O. Polat, “Optically switchable fluorescence enhancement at critical interparticle distances,” *Adv. Theory Simul.*, vol. 8, no. 9, p. 202501134, 2025.

Supplementary Information for
Geometry-Controlled Excitonic Emission Engineering in Monolayer MoS₂
Using Plasmonic Hollow Nanocavities

Abdullah Efe Yildiz^{1,2} and Emre Ozan Polat^{1,2,*}

¹*Department of Physics, Bilkent University, 06800, Ankara, Turkey*

²*UNAM - National Nanotechnology Research Center and Institute of Materials Science and Nanotechnology, Bilkent University, Ankara 06800, Turkey*

**Corresponding author: emre.polat@bilkent.edu.tr*

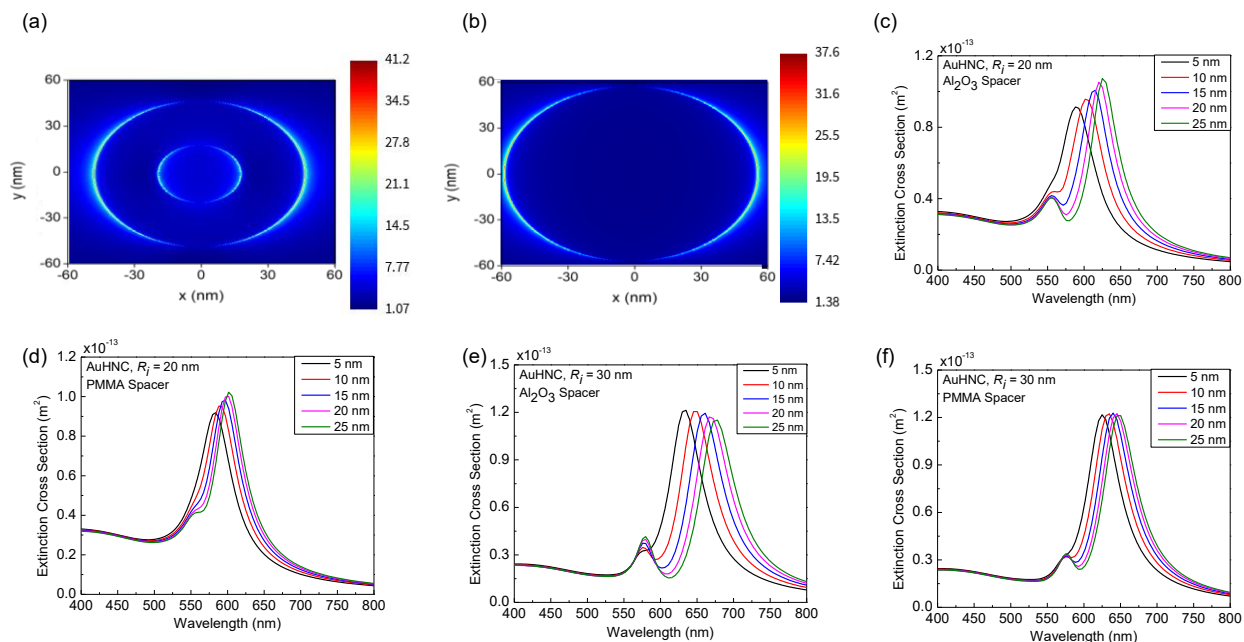
The supplementary figures provide additional numerical results supporting the plasmon-exciton interaction analysis presented in the main text.

Supplementary Figure S1. Electric-field confinement and geometry-dependent plasmonic response of hollow nanocavities.

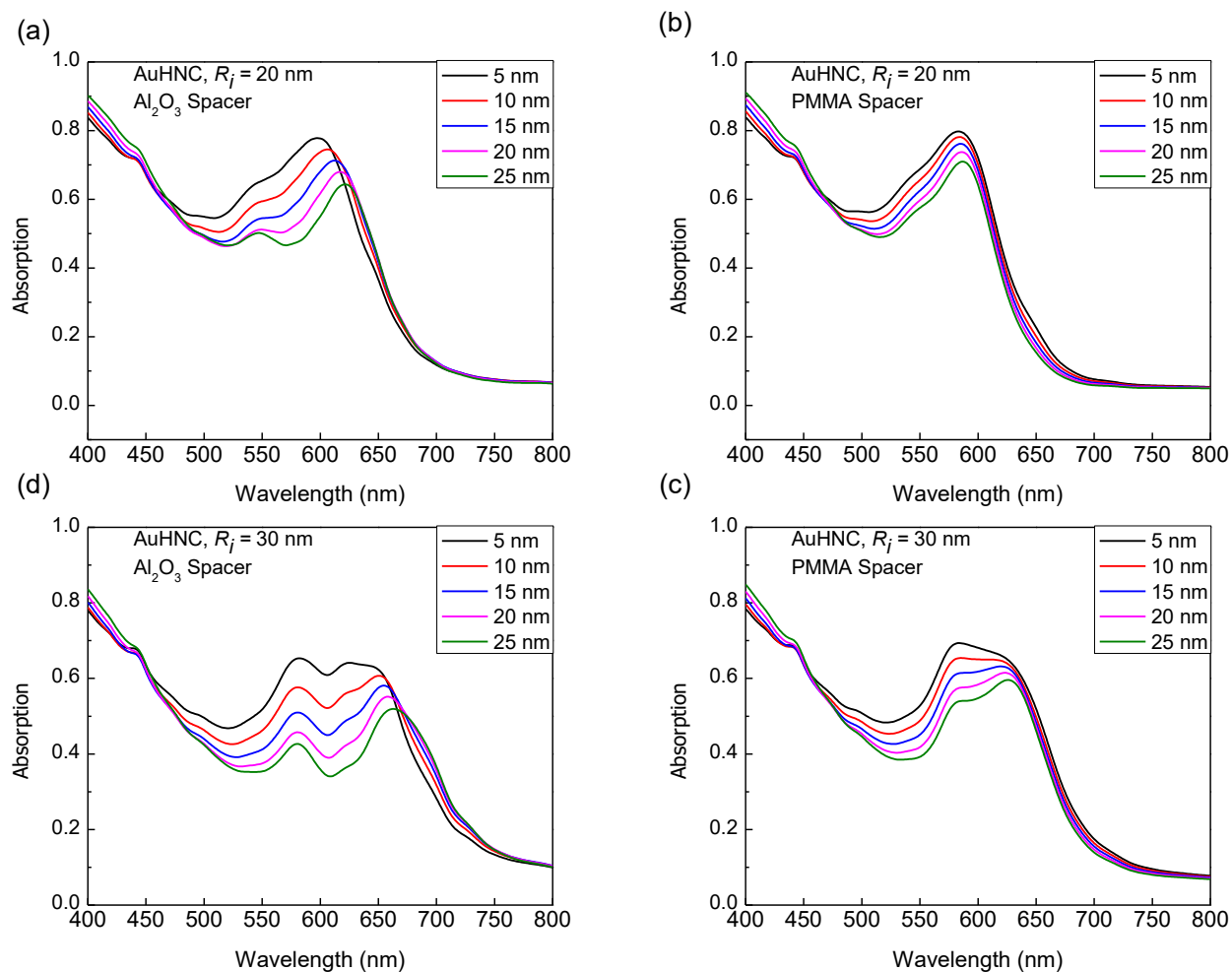
Supplementary Figure S2. Spacer-dependent absorption response of AuHNC-MoS₂ hybrid structures.

Supplementary Figure S3. Charge-generation-rate (CGR) spectra of AuHNC-MoS₂ hybrid systems.

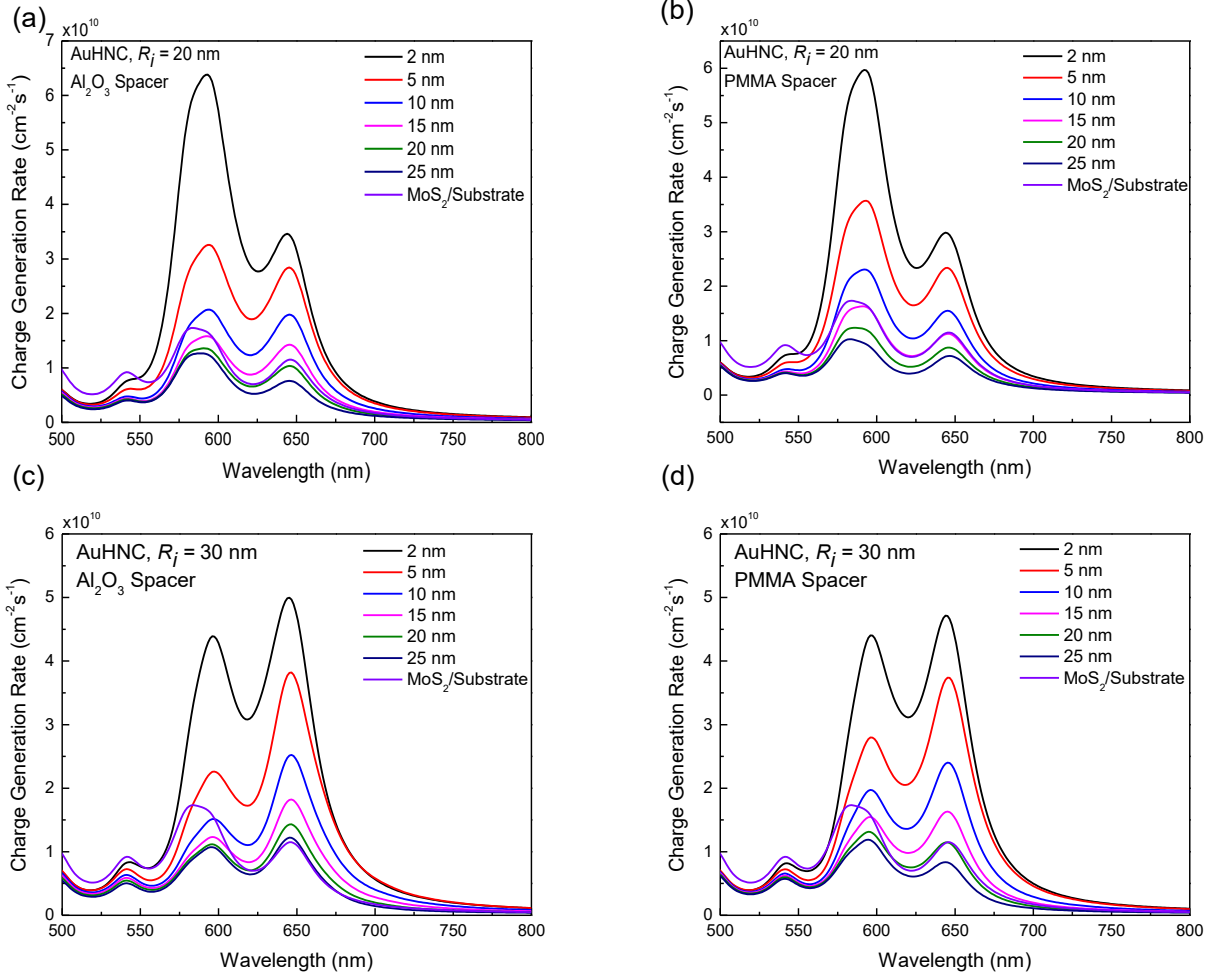
Supplementary Figure S4. Spacer-dependent quantum efficiency of AuHNC-MoS₂ hybrid structures.



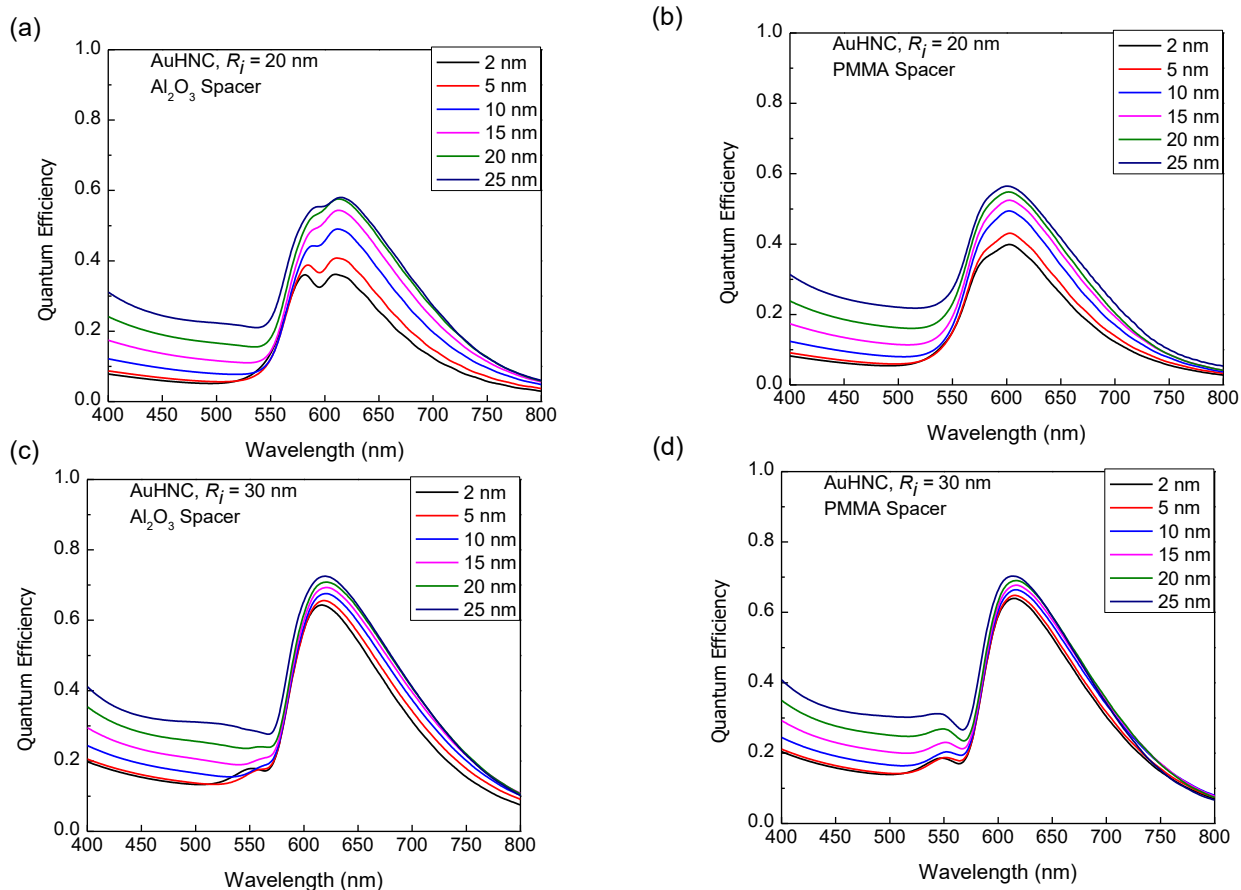
Supplementary Figure S1. Electric-field confinement and geometry-dependent plasmonic response of hollow nanocavities. (a) Simulated electric-field intensity distribution ($|E|^2$) in the x - y plane for a hollow gold nanocylinder (AuHNC), showing strong field localization at both the inner and outer cavity boundaries arising from hybridized radial-longitudinal plasmon modes. (b) Corresponding electric-field distribution for a solid gold nanocylinder, where the field is primarily confined along the outer perimeter, illustrating the reduced modal confinement compared with the hollow structure. (c–f) Extinction spectra for selected geometries corresponding to different cavity aspect ratios (CARs) designed to spectrally align the plasmon resonance with the B (c,d) and A (e,f) excitonic transitions of monolayer MoS₂ for Al₂O₃ and PMMA spacer environments.



Supplementary Figure S2. Spacer-dependent absorption response of AuHNC-MoS₂ hybrid structures. (a) Absorption spectra of the hybrid structure with an Al₂O₃ spacer for geometries engineered to spectrally overlap with the B exciton of monolayer MoS₂. (b) Corresponding absorption spectra for a PMMA spacer targeting the B-exciton transition. (c) Absorption spectra for the Al₂O₃ spacer case with cavity geometries designed to align the plasmon resonance with the A exciton. (d) Corresponding absorption spectra for the PMMA spacer configuration targeting the A-exciton transition.



Supplementary Figure S3. Charge-generation-rate (CGR) spectra of AuHNC-MoS₂ hybrid systems. (a) CGR spectra for hybrid structures with an Al₂O₃ spacer designed to spectrally target the B exciton of monolayer MoS₂. (b) Corresponding CGR spectra for a PMMA spacer tuned to the B-exciton transition. (c) CGR spectra for the Al₂O₃ spacer configuration engineered to align the plasmonic resonance with the A exciton. (d) CGR spectra for the PMMA spacer configuration targeting the A-exciton transition. In each panel, the spacer thickness varies from **2 to 25 nm**, demonstrating how the separation between the Au hollow nanocylinder and the MoS₂ layer modifies the near-field interaction and consequently the exciton charge-generation rate. The response of the bare MoS₂/substrate system is shown for comparison.



Supplementary Figure S4. Spacer-dependent quantum efficiency of AuHNC-MoS₂ hybrid structures. (a,b) Quantum-efficiency spectra for geometries designed to target the B exciton of monolayer MoS₂ with Al₂O₃ and PMMA spacers, respectively. (c,d) Corresponding quantum-efficiency spectra for geometries engineered to align the plasmonic resonance with the A exciton for Al₂O₃ and PMMA spacer layers. In each panel, the spacer thickness varies from **2 to 25 nm**, illustrating how the separation between the hollow gold nanocylinder and the MoS₂ layer regulates the balance between radiative enhancement and non-radiative energy transfer to the metal.